frontiers
in Earth Science

ORIGINAL RESEARCH
published: 25 November 2021
doi: 10.3389/feart.2021.774200

Emergency Survey and Stability Analysis of a Rainfall-Induced Soil-Rock Mixture Landslide at Chongqing City, China

Chang Zhou[1], Dong Ai[2], Wei Huang[2], Huiyuan Xu[2], Liwen Ma[2], Lichuan Chen[3] and Luqi Wang[4]*

[1]School of Resources and Geosciences, China University of Mining and Technology, Xuzhou, China, [2]The Seventh Geological Brigade of Hubei Geological Bureau, Yichang, China, [3]Chongqing Engineering Research Center of Automatic for Geological Hazards, Chongqing Institute of Geology and Mineral Resources, Chongqing, China, [4]School of Civil Engineering, Chongqing University, Chongqing, China

The stability analysis of damaged landslides and unstable debris is important for rescue work and emergency operations. This paper investigates a predisposed geological emergence, inducing the factors and deformation processes of the Zhongbao landslide, which happened on July 25, 2020. The stability of the landslide debris was evaluated by an integrated monitoring system consisting of ground-based radar, unmanned aerial vehicles, airborne Lidar, thermal infrared temperature monitoring, GNSS displacement monitoring, deep displacement monitoring, and rainfall monitoring. The strata and weak layer controlled the landslide failure, and topography defined the boundary of the failed rock mass. A continually intensive rainfall caused the deformation and accelerated failure of the landslide. The shallow and steep deposit (Part I) firstly slid at a high velocity, and then pushed the rear part of the landslide (Part II) to deform, forming numerous cracks, which accelerated the rainfall infiltrating into the rock mass. The moisture content increase could decrease the strength of the shale rock within the bedding planes. Finally, with the rock and soil mass sliding along the weak layer, a barrier dam and a barrier lake were formed. The monitoring and numerical simulation results showed that after the landslide failure, there was still local collapse and deformation occurrences which threatened rescue work and barrier lake excavation, and the stability of the accumulation area gradually decreased as the rainfall increased. Therefore, the barrier dam was not excavated until the accumulation rate gradually stabilized on July 28. Moreover, most of the reactivated deposits still accumulated in the transportation and source areas. Thus, in August, the displacement of the landslide debris gradually accelerated in a stepwise manner, and responded strongly to rainfall, especially in the accumulation area, so that it was inferred that the damaged landslide could slide again and cause a more threatening and severe failure. The analysis results of the study area can provide references for the failure mechanism of a rainfall-induced landslide and the stability evaluation of a damaged landslide.

Keywords: damaged landslide, emergency monitoring, rainfall, failure mechanism, thermal infrared temperature

Edited by:
Yun Zheng,
Institute of Rock and Soil Mechanics (CAS), China

Reviewed by:
Wu Wenan,
Beijing University of Technology, China
Longlong Chen,
Politecnico di Milano, Italy

****Correspondence:***
Wei Huang
huangwei@cug.edu.cn

Specialty section:
This article was submitted to Geohazards and Georisks, a section of the journal Frontiers in Earth Science

Received: *11 September 2021*
Accepted: *19 October 2021*
Published: *25 November 2021*

Citation:
Zhou C, Ai D, Huang W, Xu H, Ma L, Chen L and Wang L (2021) Emergency Survey and Stability Analysis of a Rainfall-Induced Soil-Rock Mixture Landslide at Chongqing City, China. Front. Earth Sci. 9:774200. doi: 10.3389/feart.2021.774200

INTRODUCTION

Rainfall-induced landslides are widely distributed in the world, for example, over 2,500 landslide events were reported between 1950 and 2005 (Tohari, 2018). Rainfall increases the weight of the sliding mass, decreases the shear strength of the soil, and groundwater level change could cause dynamic and static pore pressure inside landslide (Tsai, 2008; Li et al., 2018a). As one of the most catastrophic types of landslide, the affected bedding rock has a strong sensitivity to water, because a weak structural layer is widely developed in the rock strata (Gu, 1979; Huang, 2007; Yin, 2011; Tang et al., 2019; Wang et al., 2019; Chen et al., 2020), such as in the 2008 Jiweishan landslide (Yin et al., 2011; Tang et al., 2015; Zhang et al., 2018a), 2006 Leyte landslide (Evans et al., 2007; Guthrie et al., 2009), and so on. Therefore, it is necessary to study the deformation characteristics and failure mechanism of affected bedding rock slopes triggered by rainfall.

Multi-field information is very important in understanding the deformation characteristics of a landslide. Over the last decade, some new technologies have been developed to monitor landslide deformation, such as GB-InSAR, TLS, IRT, digital photogrammetry (DP), and so on (Nicola et al., 2010; Del Ventisette et al., 2011; Bardi et al., 2014; Crosetto et al., 2016; Zin et al., 2016; Casagli et al., 2017; Li et al., 2020; Zhou et al., 2020), and have achieved remarkable achievements in monitoring, prediction, and early warning of the landslides (Xu et al., 2016; Piciullo et al., 2018; Ouyang et al., 2019). Those technologies are characterized by more efficient operation and higher accuracy of monitoring data, compared with traditional monitoring sensors: offering high-resolution image data acquisition, data diversity, device portability, and easy and fast data processing (Casagli et al., 2017). Those devices can systematically and easily update their data. However, there are few reports about using these technologies to monitor damaged landslide debris, where local deformations or further collapse can still occur and threaten rescue and emergency work.

A catastrophic landslide occurred in Chongqing, China, during July 23–27, 2020. A total of 520 persons were evacuated and two roads were damaged. A barrier lake formed and threatened the safety of over 8,500 residents downstream at the Quantang Hydropower Station and Canggou Township. Chen et al., 2021 analyzed the deformation characteristics of this landslide and believed it to be an accumulation landslide, sliding along the bedrock interface. However, new research found that three weakened layers can be observed within the landslide debris, and the deeper internal weakened layer is the sliding zone, which means that this landslide has completely different deformation characteristics. In this paper, the new investigation and monitoring results are presented. The deformation mechanism and stability of the landslide are analyzed by using some advanced technologies and numerical simulation to provide information for the barrier lake excavation and the rescue work. Uniaxial compression tests of shale samples with different bedding planes and moisture content were taken.

MATERIALS AND METHODS

Description of the Zhongbao Landslide

The Zhongbao landslide is located on the north side of the Yancang river, about 59 km to the Wulong District, Chongqing, China (**Figure 1A**). In plan view, the shape of the Zhongbao landslide can be approximately likened a tongue, being 850 m in length and 200 m in width (**Figure 1B**). The thickness of the landslide is estimated to be 25–47 m, and its' volume approximately 4.6 × 106 m^3 (**Figure 1C**). The slope of the landslide surface is 25°–45°. The main sliding direction is 210°, approximately perpendicular to the Yancang River. The Zhongbao landslide began to slide at 16:00 on July 23, 2020, accelerated and slid into the river on July 27, and destroyed three buildings and main roads. Over 1.0 × 104 m^3 of soil and rock mass slipped into the river and formed a barrier lake.

The field investigation indicates that the main geologic units of the area are deposits and shales. The uppermost part of the surficial deposits are eluvial deposits (up to 0.5~3.5 m thick), whereas stratigraphically lower layers comprise mostly alluvial deposits and colluvial deposits. The eluvial deposits consist of clay and 10~45% of gravel clasts (**Figures 2A,B**). The diameter of the gravel clasts ranges from 50 to 300 mm. *In-situ* exposed outcrops over 10 m high (undisturbed by the landslide) crop out near the western limit of the depictions of the lithological structure (**Figure 2C**). Dominant pale-yellow shales, 0.2~0.5 m thick, are found in the pelitic structure with developed joints. The main component of shales is smectite and other clay minerals, which are easily weathered and softened by water. The rocks dip 25° toward 130°. Two dominant joints are found in the study area (**Figure 2D**). The first joint dips 75° toward 5°–15° with a width of 3~15 mm and a length of 1.5–4.9 m, and the joint spacing is 1.30–4.20 m. The second one dips 80° toward 210°–230° with a width of 2–12 mm and a length of over 10 m, and the joint spacing is 1.10–2.70 m. The joints are partially filled with clay.

Landslide Monitoring After Failure

Emergency Monitoring Systems

After landslide failure, emergency work and stability evaluation of the reactivated deposits are necessary, but conventional monitoring technologies are not equipped to monitor the damaged landslide, because of the instability of the landslide and debris. Therefore, some new methods are taken to monitor the deformation of the landslide (**Figure 3**):

1) Ground-based radar

HC-GBSAR1000 ground-based radar monitoring system uses Ground-based repeated orbit interferometric SAR technology, which accurately measures the displacement of the landslide's surface by comparing different pictures at different times based on the principle of phase interference. This technology has the technical advantages of being all-weather, high-precision, and a continuous measurement in time and space. Therefore, it was used in emergency monitoring of the landslide.

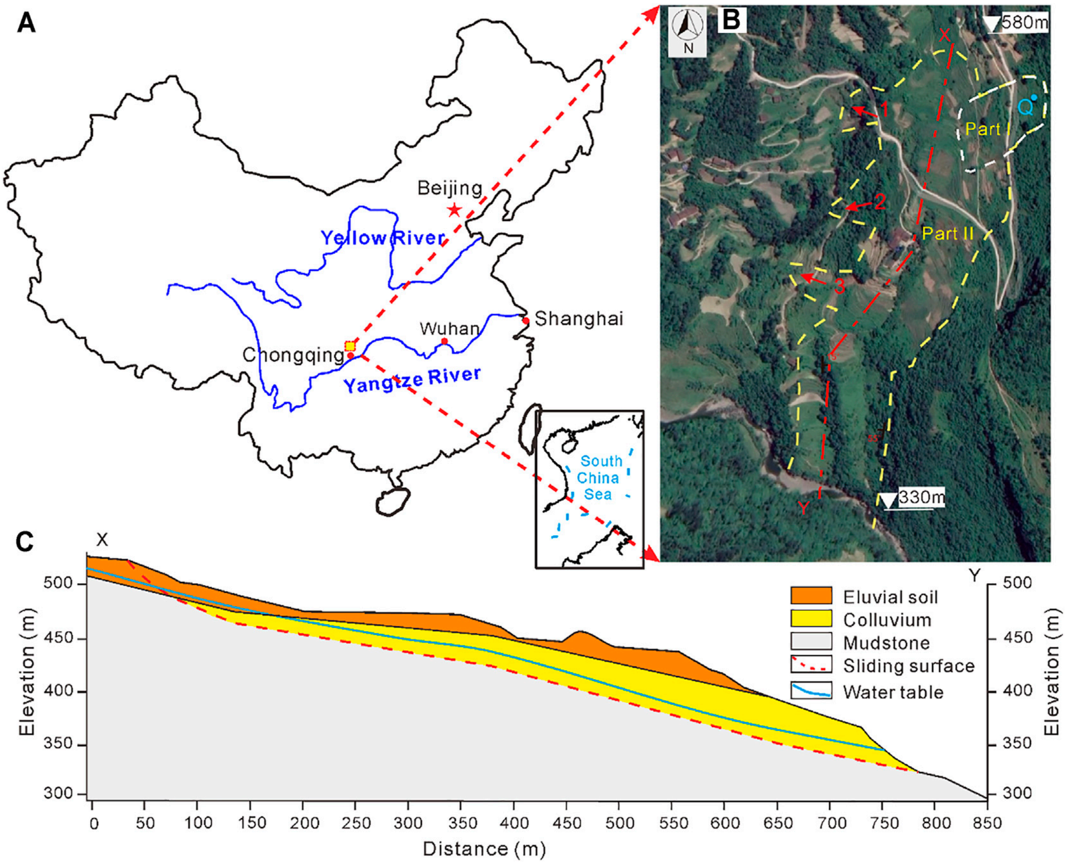

FIGURE 1 | Zhongbao landslide: **(A)** location of the landslide, **(B)** plane view and **(C)** vertical profile after landslide failure.

2) Unmanned Aerial Vehicle

Five sensors are equipped in the unmanned aerial vehicle to take pictures from five viewpoints. Meanwhile, the location of the vehicle during flight is recorded, including its height, speed, and flight direction. Based on the digital aerial stereo images, the image points and coordinates are automatically recognized, and the three-dimensional coordinate of the study objection is formed by using the analytical photogrammetry method. This technology could rapidly obtain a digital orthophoto, a digital elevation model, and high-resolution three-dimensional models, which provide fundamental data for the evaluation and monitoring of the landslide.

3) Airborne Lidar

The airborne Lidar integrates multiple technologies, such as laser, computers, high dynamic carrier attitude determination technology, and High-precision dynamic GNSS (Glogbal navigation satellite system) differential technology. This technology recognizes objects by laser technology and analyzes those data by computer technology. Airborne lidar is composed of a laser scanner system, a position and orientation system (POS) (GNSS), and a high-resolution camera system. The technology can avoid the effect of trees and obtain a high-resolution photograph and 3D point cloud data rapidly and accurately. Those data are used to analyze the deformation and the volume of the landslide.

4) Thermal infrared temperature monitoring

The thermal Infrared Camera FLIR X8400sc is a device that converts energy into an electrical signal. It has a precision of ±0.1°C, a temperature resolution of 0.04°C, a resolution of 1,280 × 1,024 pixels, and a spectral range of [1.5 5.1] μm. This equipment measures the temperature of the landslide surface so as to obtain the temperature of the field.

Conventional Monitoring Systems

Conventional monitoring equipment has been widely used in natural hazard monitoring because of its low cost, simple structure, and easy construction. In addition, they are applied for their wireless transmission of measurement data. In this paper, these monitoring technologies are used (**Figure 3**):

1) GNSS displacement monitoring

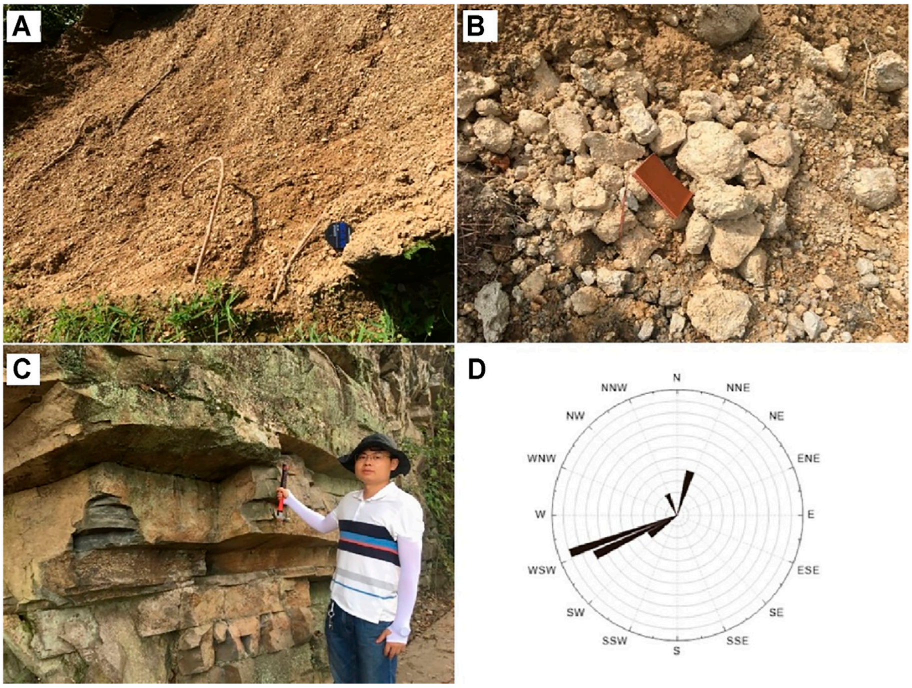

FIGURE 2 | (A) Eluvium, **(B)** gravel soil, **(C)** Hanjiadian Formation Shale (S1h), and **(D)** rose diagram of the joins.

The principle of GNSS monitoring is to determine the position of the GNSS receiver using the distance intersection method by measuring the distance between four or more satellites and receivers. The base station is constructed in a stable area, and monitoring stations are built in a deformation area. The displacements of the monitoring stations are calculated by comparing the location between the base and monitoring stations.

2) Displacement monitoring in depth

The flexible inclinometer probe, invented by Chongqing Engineering Research Center of Automatic Monitoring for Geological Hazards, measures its angle by three-dimensional micro-mechatronics measurement units (MEMS) to calculate horizontal displacement. The flexible probe monitoring system includes a flexible probe, controller, and PC software. One probe contains 80 measurement units and vertical spacing of 1.0 m. Unfortunately, the flexible probe did not work after being installed into the landslide.

3) Rainfall monitoring

A tipping bucket rain gauge was used to measure precipitation because it is characterized by real-time recording of rainfall with high accuracy and requiring almost no human factor. The measurable range of the equipment is 0.01 mm ~ 4 mm/min, and the precision is ±2%.

4) Sound and light alarm

The received data being collected and analyzed by the monitoring terminal is uploaded to a remote control terminal and then the alarm information is pushed to the sound and light warning terminal for an efficient and timely warning. Sound and light alarms are carried out in time to remind nearby vehicles and personnel to react to disasters.

RESULTS

Deformation of the Zhongbao Landslide

The Zhongbao landslide was first found to have deformed on July 22. Several cracks were recorded on the uphill side of the landslide after a continuous intense rainfall. As the landslide deformed, the eastern boundary of the landslide was generated, then a great many tension cracks formed at Part II while Part I gave way (**Figure 4B**). The uphill slope slid over 20 m, and the downhill slope suffered local deformation. On July 24, the sliding mass was transported to the middle and downhill slopes, causing the downhill slope to gradually collapse (**Figure 4C**). On July 25, there was a strong rainfall, the downslope had obvious deformation, and the sliding mass gradually slid into the Yancang River. The barrier lake and dam were formed (**Figures 4D,E**).

The steep Part I firstly deformed and collapsed, which destroyed the main road. The upstream portion of Part II gradually deformed and pushed the middle portion to slip. Due to the cliff at the east side of the landslide, the sliding direction of the landslide gradually changed from 165° in the

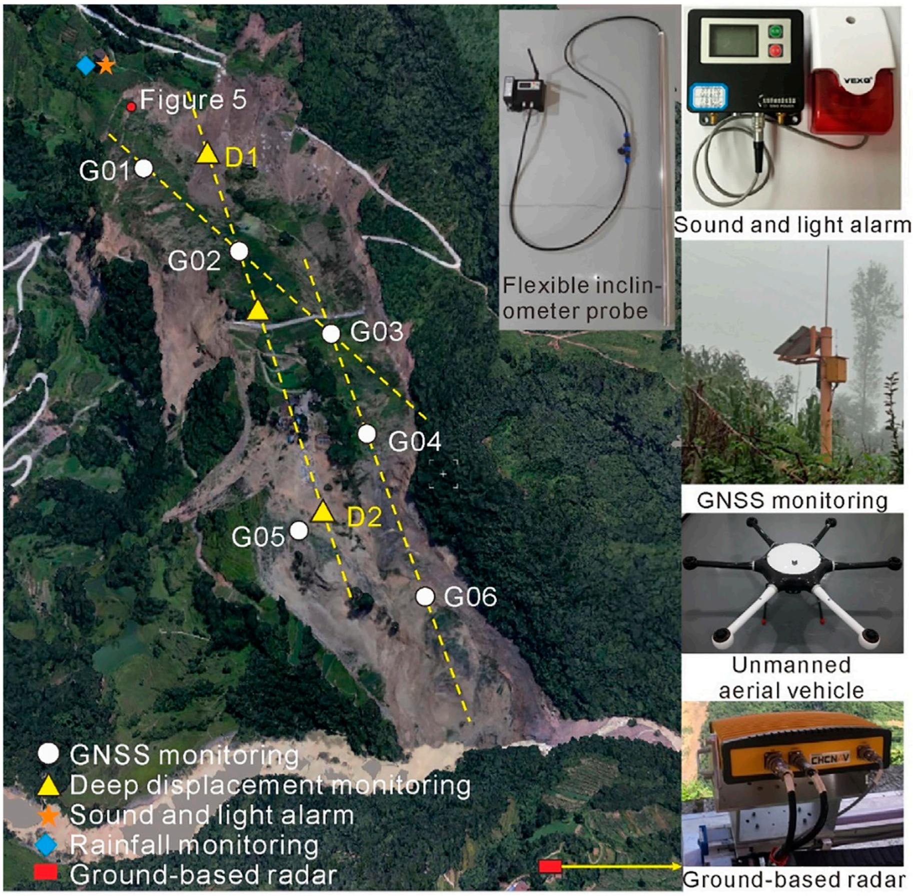

FIGURE 3 | Monitoring system of the failure landslide and photographs of the devices.

source area to 220° in the transportation area, and finally to 180° in the accumulation area. According to the deformation characteristics of the landslide, the landslide area could be divided into five areas (**Figure 9**):

Part I: This portion is located at the northeast side of the landslide (**Figure 5**). Reactivated deposits of Part I covered Part II. This part is 140–245 m wide and 230 m long, about 10 m thick with its largest elevation difference being 102 m. The deformation characteristics of the road showed that the accumulation moved with Part II, inferring that Part I failed before Part II. Due to the steep slope, engineering projection, and continual rainfall, Part I slipped with velocity and compressed Part II, which accelerated the movement of Part II. Therefore, the uplift area and puddle were found in part II.

Source area (**Figure 5**): The length and elevation difference of this area is approximately 207 and 46 m, respectively. Under the effect of rainfall and part I, the rear section of Part II gradually deformed and developed into scratch (**Figure 6A**) and tension cracks. Those cracks became an infiltration path for rainfall which damaged the yale structure and decreased the shear strength of the soil and rock. The rock became severely fragmented (**Figure 6B**). The deformation of the landslide thus accelerated. Many scarplets and cracks were found in this portion. Moreover, the boundary between the source area and the transportation area was an uplift zone with an average height of 3.0 m (**Figure 5**).

Transportation area (**Figure 7**): Owing to the rear section sliding and pushing the rock soil mass in the transportation area, some buildings and houses in the middle section only formed tension cracks but were not completely destroyed (**Figure 7**). Some parts were uplifted. In the plane view, this area had an approximately rectangular shape with a length of 340 m and an average width of 175 m. Some pools were found on the landslide. The road debris showed that it slid about 99 m but kept good continuity.

Accumulation area (**Figure 8**): The rear part became steep again, and the dip direction of the exposed rock was 15°. Thus, the sliding direction of the landslide changed. The sliding mass slipped and mobilized surficial deposits in the accumulation area by scraping, entraining, and pushing them downward. Finally, the reactivated deposits accumulated in the toe of the landslide and formed a barrier dam and barrier lake. The thermal infrared monitoring found that the temperature field appeared abnormal in the place where the groundwater was exposed. Moreover, the temperatures of the accumulation area were higher than in other areas.

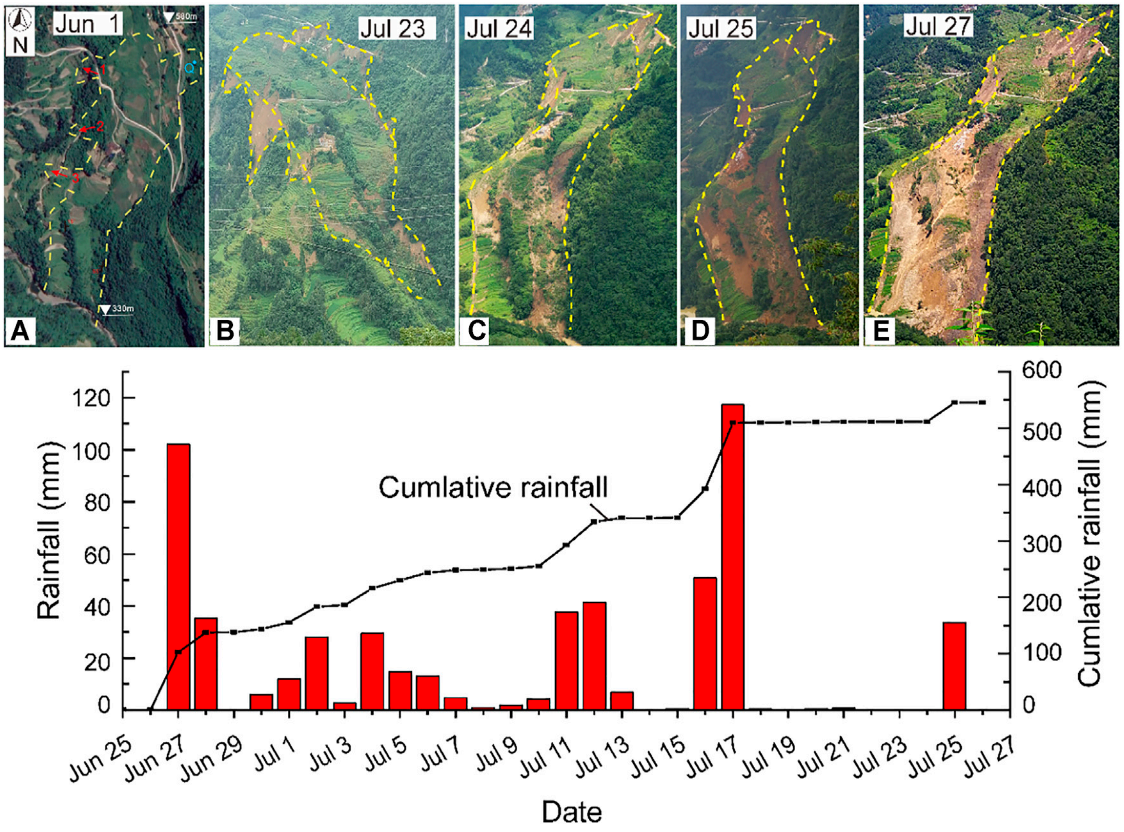

FIGURE 4 | Deformation characteristics and rainfall vs. time.

Secondary-landslide area: Three secondary-landslides (1–3# in **Figure 5**) were found at the west side of the landslide because of the V-shaped valley. No. 1 secondary-landslide was caused by the source area sliding along the direction of 230°. No. 2 is located on the cliff, so could be from the collapse of the sliding mass. No. 3, caused by a change in the sliding direction of Part II, occurred and buried a small road.

Stability of the Failure Landslide

1) Visual observation of surface deformation

The radar technology was used to evaluate the volume and deformation characteristics of the landslide because it can remove the trees on the landslide surface and obtain the rear geography of the landslide. **Figure 9** shows that Part I had an obvious boundary with 4.1 × 102 m^2. Its sliding mass accumulated in Part II and slipped to the transportation area of Part II. The downhill slope continued onto progressive retrogressive collapse and slid into the river. Thus, this landslide was still unstable. Moreover, a cliff was observed on the northeast side of the landslide with over 1 × 106 m^2 colluvial deposits where there was also the occurrence of Part I.

2) Surface displacement

An emergency monitoring was started from July 27 to Aug 2. Ground-based radar was 2.8 km away from the landslide (**Figure 3**). The surface deformation of the landslide was scanned from July 27 to October 2. Unfortunately, the monitoring was non-continuous due to the power issues and a change in the device location. Therefore, two periods are selected to analyze the deformation characteristics of the landslide debris.

Figure 10 is the monitoring results of the landslide surface from 16:00 July 27 to 06: 00 July 28. The uphill and middle of the landslide showed no obvious deformation, but the downhill section had large deformation with the largest displacement being 200 mm (**Figure 10A**). The displacements of four monitoring points in the downslope are shown in **Figure 10B**. It is observed that the displacement of P2 and P4 slowly increased and reached about 50 mm. However, the displacement at P1 and P3 had the largest values. The velocity of P1 gradually decreased after July 28. The displacement at P3 sharply increased at 22:00 July 27 and then tended to be stable. Moreover, local deformation was also found at the cliff on the northeast side of the downslope (approximately −50 mm).

Figure 11 shows the displacement of the landslide surface from 11:00 to 17:00 July 28. It was found that the largest

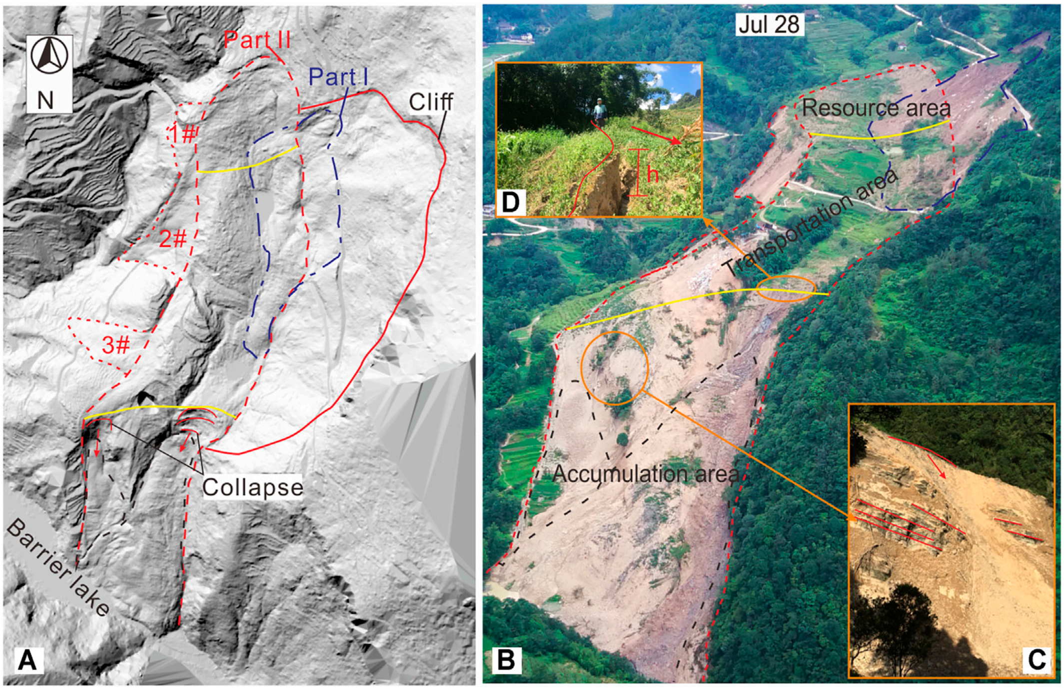

FIGURE 5 | The result of the Airborne Lidar after filtering out trees. Note the black dashed line is the secondary landslide in the accumulation area. Yellow lines separate the three parts (see text). Sub-photographs are the scarplet and local collapse, respectively.

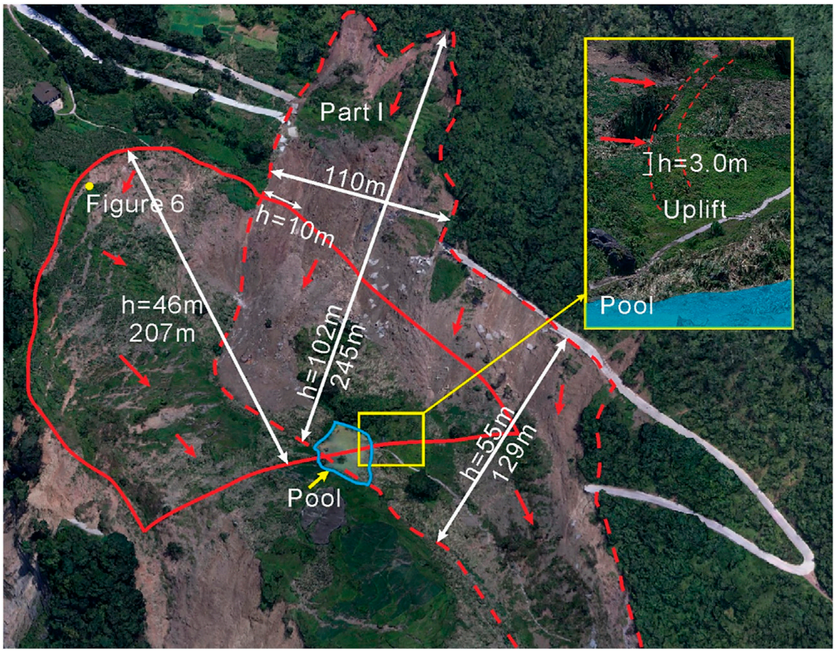

FIGURE 6 | Picture of the source area and Part I area. The sub-picture is the uplift zone between the source area (left) and the transportation area (right). Note, “h” represents the elevation difference of the landslide area.

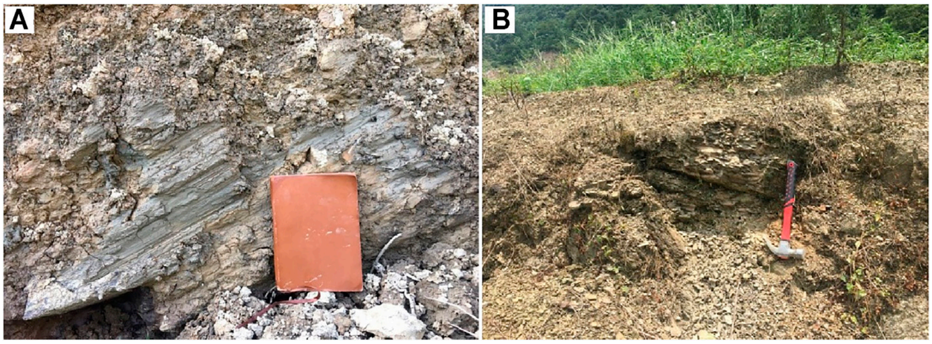

FIGURE 7 | (A) Scratch and **(B)** broken rock. See **Figure 3** for the locations of pictures.

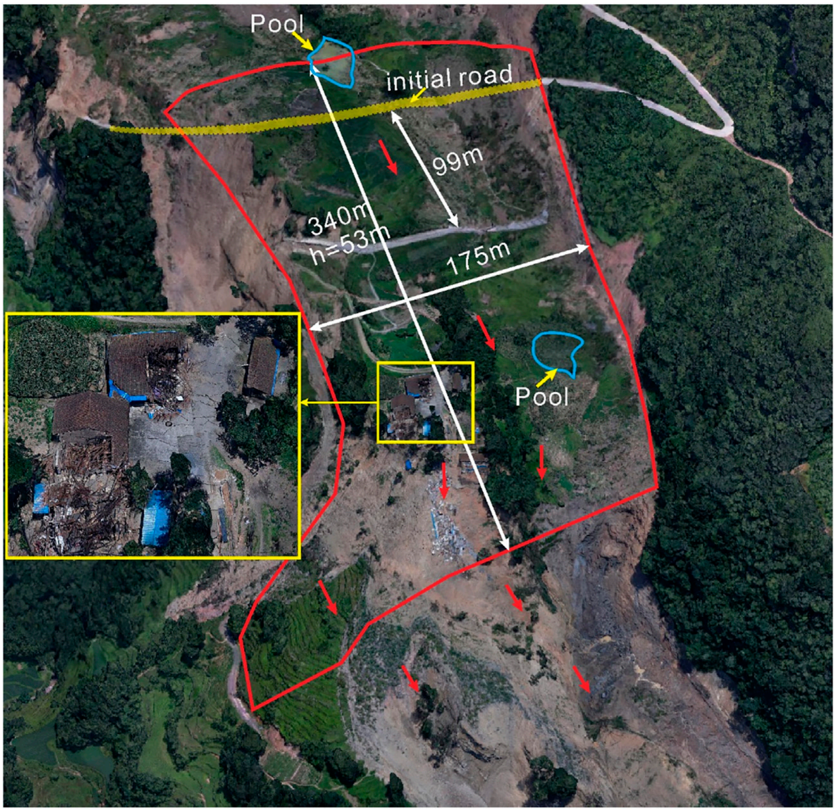

FIGURE 8 | Picture of transportation area. The sub-picture is the village which shows that most of those buildings maintain good integrity. The road also kept good continuity across two sides, even though it slid over 90 m. The blues line are pools.

displacement of the landslide is about 70 mm, which is clearly smaller than that in **Figure 10** (**Figure 11A**). The displacement of the point at P was monitored (**Figure 11B**). The displacement increases with a velocity of 12 mm/h, which indicated that local collapse was still occurring **Figure 11C** shows that the upslope also had small deformation (>40 mm) and the whole landslide was stable.

In consequence, after the landslide collapse, this landslide tended to be stable except for local collapses. The emergency works were taken in the source and transportation area before July 28, and then, the barrier dam was excavated on July 28. The traditional monitoring equipment was installed on the landslide surface.

In **Figure 12**, the rainfall and displacement from Aug 12 to Oct 1 was recorded. The second wet month (from September to October) was characterized by a 333 mm cumulative rainfall. The downhill slope (G05, G06) had large deformation with a velocity as high as 6 cm/day (G06). The increment displacement of the

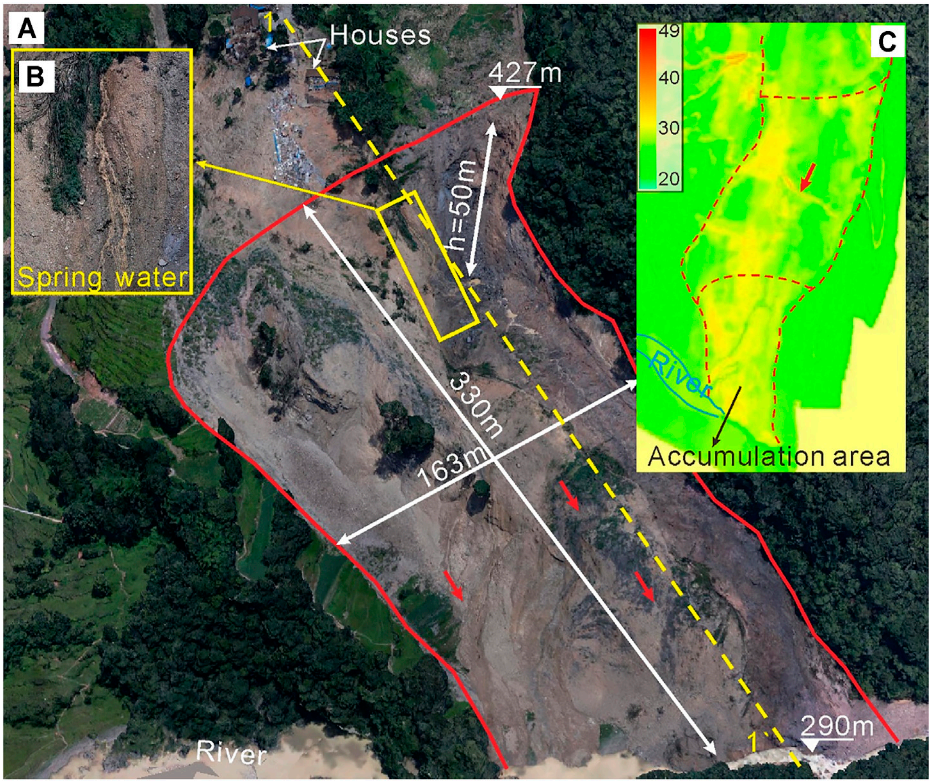

FIGURE 9 | Picture of accumulation area **(A)**, the spring water **(B)**, and the temperature of the landslide surface **(C)**.

G06 suddenly decreased tending to zero, but the G05 went on with a constant rate of 3.8 mm/day. Clearly, the rainfall reactivated the landslide. Moreover, the increase of the displacement at G06 and G05 generally lagged 1 day behind the rainfall. Another portion of the landslide had a smaller displacement (<30 mm/month), but also responded to the rainfall and gradually increased.

DISCUSSION

Failure Mechanism of the Zhongbao Landslide

Water has a significant effect on the strength of shale rock. The increase of the water content could lead to mineral particle dissolution and the increase of clay minerals. As a result, the shale structure becomes loose, the mic-cracks gradually increase, and finally, the rock degrades and softens (Feng and Ding, 2005; Cornelius et al., 2011; Zhu et al., 2015; Ling et al., 2016; Liu et al., 2016; Xue et al., 2018; Li et al., 2019). Moreover, a filed investigation found that the primary porosity of shale in the landslide area was well developed, and three sets of the superior fractures caused the loosening of the rock. Therefore, after a constant rainfall (July 15–18), the rainfall infiltrated into the landslide and decreased the shear strength of the rock. Further, underground water had a lubrication effect on the rock layers, so that the landslide began to deform on July 22. The displacement of the monitoring results also showed that the failure landslide had a large deformation after a strong rainfall (Sep 6). Moreover, the lag time of the landslide deformation after failure (about 1 day) was shorter than that of the landslide before failure response to rainfall (about 6 days), which could be because of the loose deposits after landslide collapse accelerated the rainfall infiltration. According to the deformation characteristics of the landslide, the deformation process could be divided into three stages:

Creep deformation stage: Rainfall caused a shallow landslide (Part I). A continuous rainfall lasted for almost 20 days and increased the groundwater level. As a result, the weight of the sliding mass was increased and the shear strength of the soil decreased. Moreover, the main road provided beneficial conditions for Part I failure. The reactivated deposit impacted and compressed the upslope of part II which accelerated the deformation of the landslide (**Figure 4B**). Besides, the gentle slope in the middle of the landslide is conducive to the accumulation of groundwater. Therefore, under the action of groundwater immersion, the landslide gradually moved. Thus, the scratch and shear cracks were generated at the uphill side of the landslide (**Figure 6**). The uphill section gradually generated obvious deformation. The deformation direction of part I is 230°.

Accelerated deformation stage: After the rear part of the landslide was initialized, it gradually slid along the sliding zone and compressed the middle section. Although there was no rainfall, the surface water continually infiltrated along these

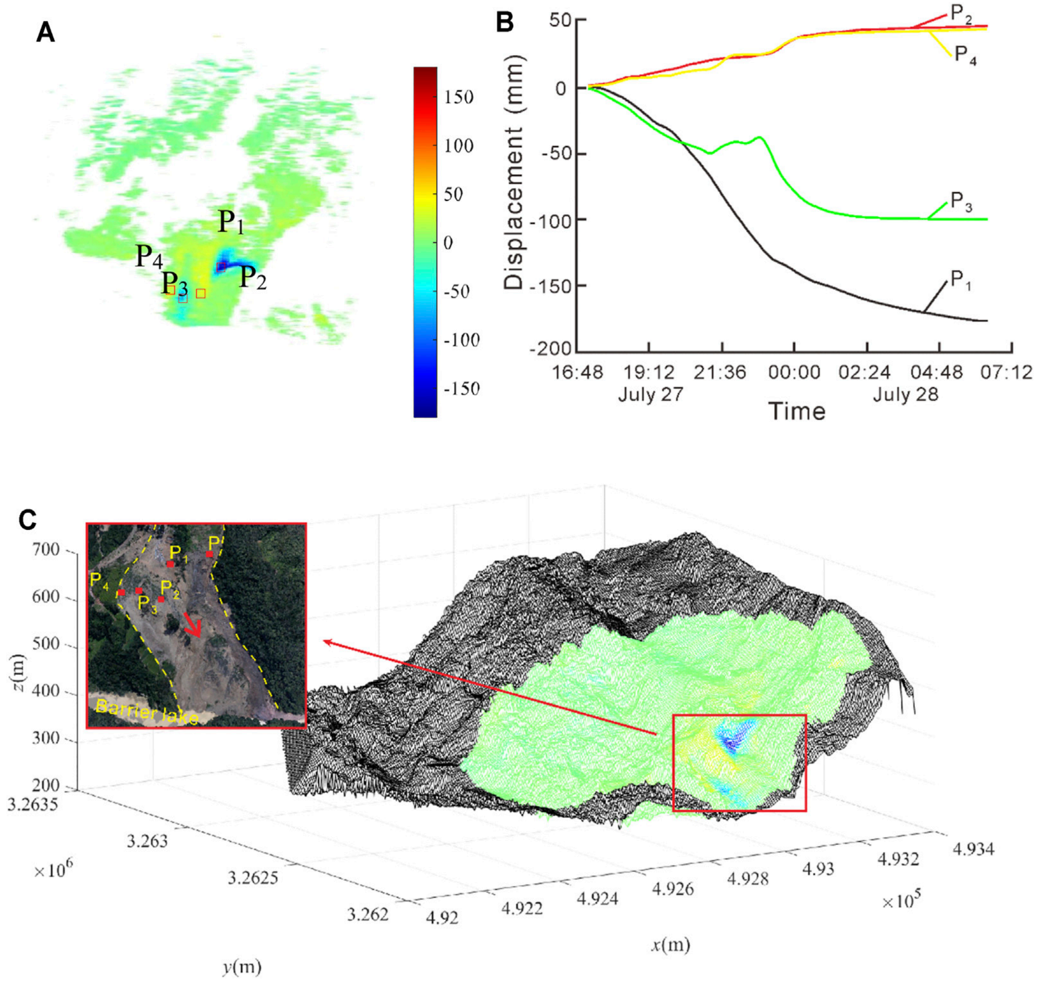

FIGURE 10 | Deformation of the Zhongbao landslide during July 27–28. **(A)** Accumulative displacement of the landslide surface; **(B)** the displacements of monitoring points vise time; **(C)** Three-dimensional topographic map. Note, the negative value of the displacement means that the point moves toward the Radar.

shear cracks, and the shear strength of the soil continually decreased under groundwater immersion. The sliding zone rapidly developed and the landslide slid over 90 m (**Figure 4C**). The sliding direction was 210°.

Accumulation stage: the landslide slides out from the steep ridge of the front edge and pushes and scrapes the shale (**Figure 4E**), which accumulates at the foot of the landslide and a barrier lake is formed. Moreover, the scarplet in front of the landslide led to the deposit mainly accumulating in the landslide toe and forming a secondary landslide (**Figure 9**) which still deformed after the landslide failure, especially when heavy rainfall occured.

The pale-yellow shale samples, with different water content and angles of bedding planes, were tested to obtain the compressive strength by uniaxial compression test (shown in **Figure 13**). All curves had the same shapes that as the water content increased, the compressive strength gradually decreased (Yang et al., 2007; Wei et al., 2015. The angle of bedding planes also had significant importance on the strength, because the clay minerals filled in the bedding plane, the content of which could be over 35% clay minerals (Fang et al., 2019), such as kaolinite, montmorillonite, illite, absorbed water and swelled, causing expansive pressure. As a result, the shale rock gradually split and disintegrated along the bedding plane (Rybacki et al., 2015; Rybacki et al., 2016; Teng et al., 2017), which also provided further seepage channels. Moreover, two clay layers (0.5–1.5 m thickness) were observed in the shale rock layer, one of which was the sliding surface. According to the other reports, the shear strength properties of the clay have a significant decrease when the moisture content increases (Dafalla, 2013; Li et al., 2018b; He et al., 2018), and are more sensitive than the rock. Therefore, after intense rainfall, the landslide slipped along the clay layer, and the shale rock was fragmented in the sliding mass.

After the landslide failed, the barrier lake formed in front of the landslide increased the groundwater level of the accumulation area (**Figure 14**). The reservoir impoundment could accelerate the landslide deformation and failure (Macfarlane, 2009; Huang et al., 2016; Li et al., 2018b; Wang et al., 2019). When the lake flooded the downhill portion of the deposit, the shear resistance was reduced (He et al., 2018), especially for the destroyed

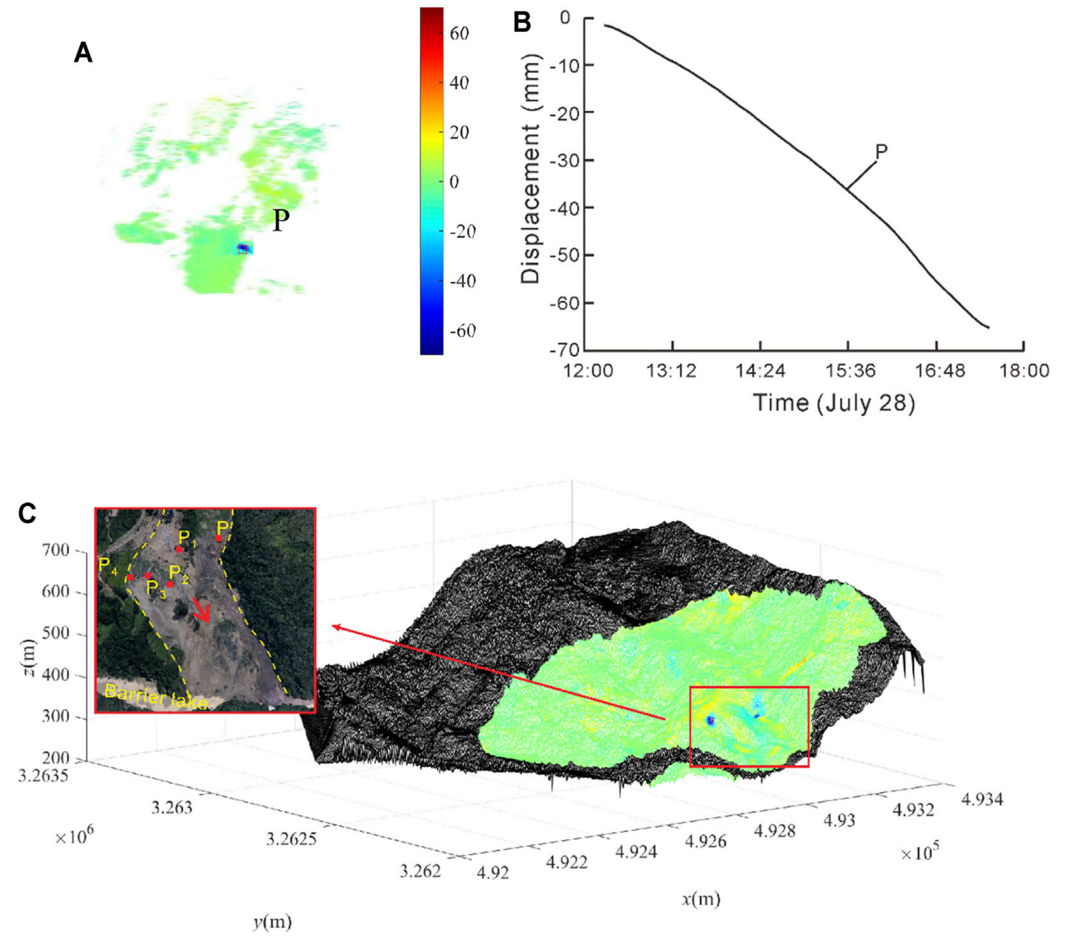

FIGURE 11 | Deformation of the Zhongbao landslide during July 28. **(A)** Accumulative displacement of the landslide surface; **(B)** the displacements of monitoring points vise time; **(C)** Three-dimensional topographic map.

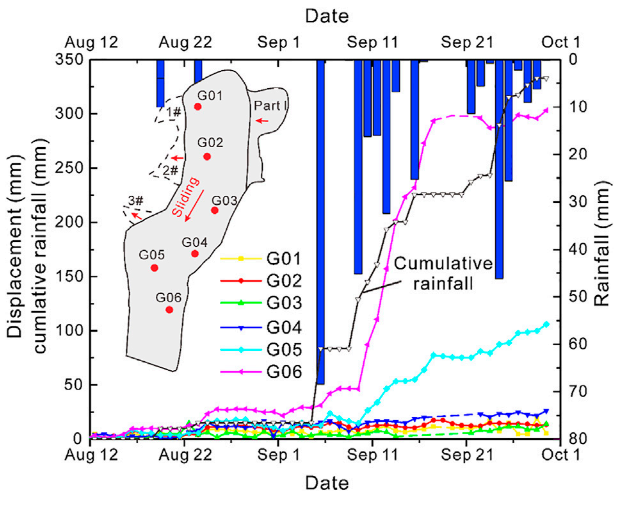

FIGURE 12 | Rainfall cumulative displacement of monitoring points and vs. time.

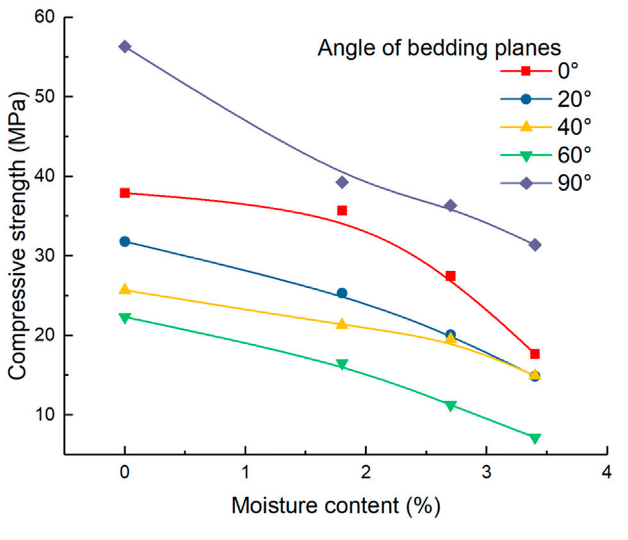

FIGURE 13 | Influence of moisture content on the compressive strength of the shales with different angles of bedding planes.

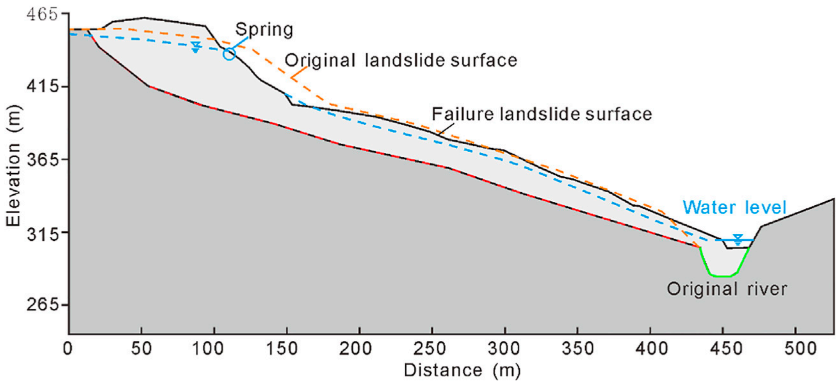

FIGURE 14 | Profile 1–1′ of the accumulation area (shown in **Figure 9**).

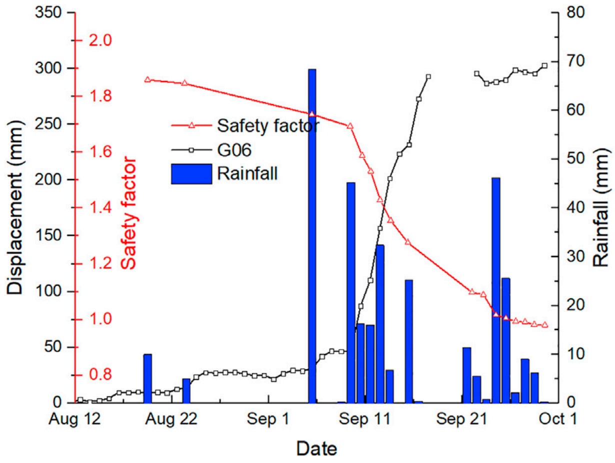

FIGURE 15 | Safety factor of the accumulation area.

deposits, so that the deposit still had a strong response to the rainfall. In the collapse at the shear outlet of the landslide, several springs with a flow velocity of 0.1–0.6 m^3/s indicated that the seepage field rapidly declined which could decrease the stability of the landslide (Berilgen, 2007; Della Seta et al., 2013; Hu et al., 2017; Sui and Zheng, 2017; Zhang et al., 2018b; Wu et al., 2020; Yang et al., 2020). The stability of the accumulation area was evaluated using Geo-slope software. Firstly, we evaluated the safety factor of the accumulation area under rainfalls (**Figure 15**). The safety factor of the accumulation area had a strong response to the rainfall and presented a certain linear change as the displacement increased. During an intensity continuous rainfall, the safety factor significantly decreases, because the groundwater level rapidly increases. If the dammed lake is excavated and drained during this stage, the landslide could slide again and form a larger barrier dam.

Emergency Monitoring System for the Damaged Landslide

After landslide failure, the re-activated deposit and the barrier lake could cause secondary economic losses (Fan et al., 2015; Gischig et al., 2016; Liu et al., 2020), so emergency engineering is necessary (Xiao et al., 2021). This paper constructed an integrated monitoring system for landslide failure. The monitoring equipment is non-contact measurements such as Ground-based radar, Unmanned Aerial Vehicles, Airborne Lidar, and thermal infrared temperature monitoring. These devices can scan the whole landslide surface and obtain point cloud data to evaluate the stability of the landslide debris in detail. The monitoring results found that deformation mainly occurred in the scarp at the uphill side of the landslide, and the deformation gradually tend to become stable after July 28. Those results provided guidance for rescue work and the excavation of barrier lakes. However, these devices are too expensive and difficult to operate if used for long-term monitoring of landslides, and also in addition only obtain deformation information of the landslide surface. Therefore, After landslide failure gradually stableizes, conventional sensors should be installed into the landslide to measure the displacement of the typical landslide profiles, such as GNSS, GPS, deep monitoring, and so on. Those devices can measure the multi-filed information of the landslide for a long time without interruption, which could provide information for reconstruction work. In this paper, the monitoring for the failing landslide shows that the failing landslide debris is still responsive to rainfall, especially at the front and middle parts of the landslide. Thus, engineering activities and human activity should be avoided as far as possible in the middle and front parts as the landslide could slip again and form a dammed lake. Moreover, over 1 × 106 m^2 of colluvial deposits on the northeast side of the landslide could be initialized and fail under the long-term effects of rainfall, which could cause extensive damage to the landslide. Therefore, the most effective monitoring method is non-contact devices, such as ground-based radar, unmanned air vehicles, three-dimensional laser scanners, and so on.

CONCLUSION

The Zhongbao landslide is a typical rainfall-induced landslide in the Yancang River area, situated in the Wulong District, Chongqing, China. It most likely originated catastrophically as a rockslide combined with a shallow landslide. The shallow soil slope, located in the uphill side of the landslide was triggered by continuous torrential rain, which pushed the rear part of the landslide to deform and accelerated rainfall infiltration into the landslide. The increase of the water content decreased the strength of the shale rock and made the rock more broken. The landslide gradually slid along the weak layer within the rock layer and formed a barrier lake. Moreover, the accumulation area was still deformed.

After the landslide failure, an emergency monitoring system with multiple monitoring devices was constructed to measure the deformation of the whole landslide surface. The monitoring results provided some advice for emergency engineering. The compromised landslide gradually became stable after July 28. Then, some conventional monitoring methods were installed into the landslide and the results found that the reactivated deposits still responded to rainfall.

DATA AVAILABILITY STATEMENT

The original contributions presented in the study are included in the article/Supplementary Material, further inquiries can be directed to the corresponding author.

ETHICS STATEMENT

Written informed consent was obtained from the relevant individuals for the publication of any potentially identifiable images or data included in this article.

AUTHOR CONTRIBUTIONS

The work was carried out in collaboration between all the authors. LC and LM designed the monitoring system and provided the monitoring data; WH, HX, LC taken the investigation; CZ wrote the original draft; CZ, HX, LW, and DA reviewed and edited the draft. All authors have read and agreed to the published version of the manuscript.

FUNDING

This study was financially supported by the National Key Research and Development Program of China (Grant No. 2017YFC1501303); Key Research and Development Program of Xinjiang Uygur Autonomous Region (Grant No. 2021B03004-3); Chongqing Technology Innovation and Application Development Special Key Projects (cstc2019jscx-tjsbX0015).

ACKNOWLEDGMENTS

The authors appreciate the work of the Chengdu University of Technology for providing the data of the thermal infrared temperature monitoring. All support is gratefully acknowledged.

REFERENCES

Bardi, F., Frodella, W., Ciampalini, A., Bianchini, S., Del Ventisette, C., Gigli, G., et al. (2014). Integration between Ground Based and Satellite SAR Data in Landslide Mapping: The San Fratello Case Study. *Geomorphology* 223, 45–60. doi:10.1016/j.geomorph.2014.06.025

Berilgen, M. M. (2007). Investigation of Stability of Slopes under Drawdown Conditions. *Comput. Geotechnics* 34, 81–91. doi:10.1016/j.compgeo.2006.10.004

Casagli, N., Tofani, V., Morelli, S., Frodella, W., Ciampalini, A., Raspini, F., et al. (2017). Remote Sensing Techniques in Landslide Mapping and Monitoring, Keynote Lecture. *Geoenvironmental Disasters* 4, 1–19. doi:10.1007/978-3-319-53487-9_1

Chen, L. C., Yang, H. Q., and Song, K. L. (2021). Failure Mechanisms and Characteristics of the Zhongbao Landslide at Liujing Village, Wulong, China[J]. *Landslides* 275, 1–30. doi:10.1007/s10346-020-01594-1

Chen, L., Zhang, W., Zheng, Y., Gu, D., and Wang, L. (2020). Stability Analysis and Design Charts for Over-dip Rock Slope against Bi-planar Sliding. *Eng. Geology.* 275, 105732. doi:10.1016/j.enggeo.2020.105732

Cornelius, F., Stephan, K., Wang, J. W., and Reiner, D. (2011). Weathering of Fruchtschiefer Building Stones: mineral Dissolution or Rock Disaggregation?[J]. *Environ. Earth Sci.* 63, 7–8. doi:10.1007/s12665-011-0986-z

Crosetto, M., Monserrat, O., Cuevas-González, M., Devanthéry, N., and Crippa, B. (2016). Persistent Scatterer Interferometry: A Review. *ISPRS J. Photogrammetry Remote Sensing* 115, 78–89. doi:10.1016/j.isprsjprs.2015.10.011

Dafalla, M. A. (20132013). Effects of Clay and Moisture Content on Direct Shear Tests for Clay-Sand Mixtures. *Adv. Mater. Sci. Eng.* 2013, 1–8. doi:10.1155/2013/562726

Del Ventisette, C., Intrieri, E., Luzi, G., Casagli, N., Fanti, R., and Leva, D. (2011). Using Ground Based Radar Interferometry during Emergency: the Case of the A3 Motorway (Calabria Region, Italy) Threatened by a Landslide. *Nat. Hazards Earth Syst. Sci.* 11, 2483–2495. doi:10.5194/nhess-11-2483-2011

Della Seta, M., Martino, S., and Scarascia Mugnozza, G. (2013). Quaternary Sea-Level Change and Slope Instability in Coastal Areas: Insights from the Vasto Landslide (Adriatic Coast, central Italy). *Geomorphology* 201, 462–478. doi:10.1016/j.geomorph.2013.07.019

Evans, S. G., Guthrie, R. H., Roberts, N. J., and Bishop, N. F. (2007). The Disastrous 17 February 2006 Rockslide-Debris Avalanche on Leyte Island, Philippines: a Catastrophic Landslide in Tropical Mountain Terrain. *Nat. Hazards Earth Syst. Sci.* 7, 89–101. doi:10.5194/nhess-7-89-2007

Fan, L., Lehmann, P., and Or, D. (2015). Effects of Hydromechanical Loading History and Antecedent Soil Mechanical Damage on Shallow Landslide Triggering. *J. Geophys. Res. Earth Surf.* 120, 1990–2015. doi:10.1002/2015jf003615

Fang, Z. W., Zhang, S. P., Liu, H. M., Teng, J. B., and Zhu, L. P. (2019). Bedding Structure Characteristics and the Storage Controlling Factors of Mud-Shale in Upper Es4 to Lower Es3 Members in Jiyang Depression [J]. *Pet. Geology. Recovery Efficiency* 26 (1), 101–108. doi:10.13673/j.cnki.cn37-1359/te.2019.01.011

Feng, X. T., and Ding, W. X. (2005). Meso-mechanical experiment of Micro-fracturing Process of Rock under Coupled Mechanical-Hydrological Chemical Environment[J]. *Chin. J. Rock Mech. Eng.* 24 (9), 1465–1473. doi:10.3321/j.issn:1000-6915.2005.09.002

Gischig, V., Preisig, G., and Eberhardt, E. (2016). Numerical Investigation of Seismically Induced Rock Mass Fatigue as a Mechanism Contributing to the Progressive Failure of Deep-Seated Landslides. *Rock Mech. Rock Eng.* 49, 2457–2478. doi:10.1007/s00603-015-0821-z

Gu, D. Z. (1979). *Foundation of Rock Mass Engineering geomechanics[M]*. Beijing: Science Press.

Guthrie, R. H., Evans, S. G., Catane, S. G., Zarco, M. A. H., and Saturay, R. M. (2009). The 17 February 2006 Rock Slide-Debris Avalanche at Guinsaugon Philippines: a Synthesis. *Bull. Eng. Geol. Environ.* 68, 201–213. doi:10.1007/s10064-009-0205-2

He, C., Hu, X., Tannant, D. D., Tan, F., Zhang, Y., and Zhang, H. (2018). Response of a Landslide to Reservoir Impoundment in Model Tests. *Eng. Geology.* 247, 84–93. doi:10.1016/j.enggeo.2018.10.021

Hu, X., Tan, F., Tang, H., Zhang, G., Su, A., Xu, C., et al. (2017). *In-situ* Monitoring Platform and Preliminary Analysis of Monitoring Data of Majiagou Landslide with Stabilizing Piles. *Eng. Geology.* 228, 323–336. doi:10.1016/j.enggeo.2017.09.001

Huang, Q. X., Wang, J. L., and Xue, X. (2016). Interpreting the Influence of Rainfall and Reservoir Infilling on a Landslide. *Landslide* 13, 1139–1149.

Huang, R. Q. (2007). Large-scale Landslides and Their Sliding Mechanisms in China since the 20th Century[J]. *China J. Rock Mech. Eng.* 26, 433–454.

Li, C., Wang, M., and Liu, K. (2018a). A Decadal Evolution of Landslides and Debris Flows after the Wenchuan Earthquake. *Geomorphology* 323, 1–12. doi:10.1016/j.geomorph.2018.09.010

Li, S., Sun, Q., Zhang, Z., and Luo, X. (2018b). Physical Modelling and Numerical Analysis of Slope Instability Subjected to Reservoir Impoundment of the Three Gorges. *Environ. Earth Sci.* 77 (4). doi:10.1007/s12665-018-7321-x

Li, Y. S., Jiao, Q. S., Hu, X. H., Li, Z. L., Li, B., Jingfa, Z., et al. (2020). Detecting the Slope Movement after the 2018 Baige Landslides Based on Ground-Based and Space-Borne Radar Observations[J]. *Eng. Geology.* 84, 1–12. doi:10.1016/j.enggeo.2017.09.001

Li, Z. B., Huang, T. M., Pang, Z. H., Xiong, D. M., Li, Y. M., Tian, J., et al. (2019). Study on Groundwater Baseline Quality, Monitoring Indicators and Contamination Tracing Methods Related to Shale Gas Development: a Case Study in the Fulling Gas Field in SW China[J]. *J. Eng. Geology.* 27 (1), 170–177. doi:10.13544/j.cnki.jeg.2019-056

Ling, S. X., Wu, X. Y., Sun, C. W., Liao, X., Ren, Y., and Li, X. N. (2016). Experimental Study of Chemical Damage and Mechanical Deterioration of Black Shale Due to Water-Rock Chemical Action[J]. *J. Exp. Mech.* 31 (4), 511–524. doi:10.7520/1001-4888-15-241

Liu, J., Xu, Q., Wang, S., Siva Subramanian, S., Wang, L., and Qi, X. (2020). Formation and Chemo-Mechanical Characteristics of Weak clay Interlayers between Alternative Mudstone and sandstone Sequence of Gently Inclined Landslides in Nanjiang, SW China. *Bull. Eng. Geol. Environ.* 79, 4701–4715. doi:10.1007/s10064-020-01859-y

Liu, X., Zeng, W., Liang, L., and Xiong, J. (2016). Experimental Study on Hydration Damage Mechanism of Shale from the Longmaxi Formation in Southern Sichuan Basin, China. *Petroleum* 2, 54–60. doi:10.1016/j.petlm.2016.01.002

Macfarlane, D. F. (2009). Observations and Predictions of the Behaviour of Large, Slow-Moving Landslides in Schist, Clyde Dam Reservoir, New Zealand. *Eng. Geology.* 109, 5–15. doi:10.1016/j.enggeo.2009.02.005

Nicola, C., Filippo, C., Chiara, D. V., and Guido, L. (2010). Monitoring, Prediction, and Early Warning Using Ground-Based Radar Interferometry[J]. *Landslides* 7, 291–301. doi:10.1007/s10346-010-0215-y

Ouyang, C., Zhao, W., An, H., Zhou, S., Wang, D., Xu, Q., et al. (2019). Early Identification and Dynamic Processes of ridge-top Rockslides: Implications from the Su Village Landslide in Suichang County, Zhejiang Province, China. *Landslides* 16, 799–813. doi:10.1007/s10346-018-01128-w

Piciullo, L., Calvello, M., and Cepeda, J. M. (2018). Territorial Early Warning Systems for Rainfall-Induced Landslides. *Earth-Science Rev.* 179, 228–247. doi:10.1016/j.earscirev.2018.02.013

Rybacki, E., Reinicke, A., Meier, T., Makasi, M., and Dresen, G. (2015). What Controls the Mechanical Properties of Shale Rocks? - Part I: Strength and Young's Modulus. *J. Pet. Sci. Eng.* 135, 702–722. doi:10.1016/j.petrol.2015.10.028

Rybacko, E., Meier, T., and Dresen, G. (2016). What Controls the Mechanical Properties of Shale Rocks[J]. *J. Pet. Sci. Eng.* 144, 39–58. doi:10.1016/j.petrol.2016.02.022

Sui, W., and Zheng, G. (2017). An Experimental Investigation on Slope Stability under Drawdown Conditions Using Transparent Soils. *Bull. Eng. Geol. Environ.* 77, 977–985. doi:10.1007/s10064-017-1082-8

Tang, H., Zou, Z., Xiong, C., Wu, Y., Hu, X., Wang, L., et al. (2015). An Evolution Model of Large Consequent Bedding Rockslides, with Particular Reference to the Jiweishan Rockslide in Southwest China. *Eng. Geology.* 186, 17–27. doi:10.1016/j.enggeo.2014.08.021

Tang, J., Dai, Z., Wang, Y., and Zhang, L. (2019). Fracture Failure of Consequent Bedding Rock Slopes after Underground Mining in Mountainous Area. *Rock Mech. Rock Eng.* 52, 2853–2870. doi:10.1007/s00603-019-01876-8

Teng, J. Y., Tang, J. X., Zhang, Y. N., Duan, J. C., and Wang, J. B. (2017). Damage Process and Characteristics of Layered Water-Bearing Shale under Uniaxial Compression [J]. *Rock and soil Mechanism* 38 (6), 1629–1638+1646. doi:10.16285/j.rsm.2017.06.011

Tohari, A. (2018). Study of Rainfall-Induced Landsldie: A Review. *IOP Conference Series: Earth and Environmental Science.* 118, 1–7. doi:10.1088/1755-1315/118/1/012036

Tsai, T.-L. (2008). The Influence of Rainstorm Pattern on Shallow Landslide. *Environ. Geol.* 53 (7), 1563–1569. doi:10.1007/s00254-007-0767-x

Wang, L. Q., Yin, Y. P., Huang, B. L., and Dai, Z. W. (2019). Damage Evolution and Stability Analysis of the Jianchuandong Dangerous Rock Mass in the Three Gorges Reservoir Area. *Eng. Geology.* 265, 105439.

Wu, W., Yang, Y., and Zheng, H. (2020). Hydro-mechanical Simulation of the Saturated and Semi-saturated Porous Soil-Rock Mixtures Using the Numerical Manifold Method. *Comp. Methods Appl. Mech. Eng.* 370, 113238. doi:10.1016/j.cma.2020.113238

Xiao, T., Huang, W., Deng, Y., Tian, W., and Sha, Y. (2021). Long-Term and Emergency Monitoring of Zhongbao Landslide Using Space-Borne and Ground-Based InSAR. *Remote Sensing* 13, 1578. doi:10.3390/rs13081578

Xu, Q., Liu, H., Ran, J., Li, W., and Sun, X. (2016). Field Monitoring of Groundwater Responses to Heavy Rainfalls and the Early Warning of the Kualiangzi Landslide in Sichuan Basin, Southwestern China. *Landslides* 13, 1555–1570. doi:10.1007/s10346-016-0717-3

Xue, H. Q., Zhou, S. W., Jiang, Y. L., Zhang, F., Dong, Z., and Guo, W. (2018). Effects of Hydration on the Microstructure and Physical Properties of Shale[J]. *Pet. Exploration Dev.* 45 (6), 1075–1081. doi:10.1016/s1876-3804(18)30118-6

Yang, C. H., Wang, Y. Y., Li, J. G., and Gao, F. (2007). Testing Study about the Effect of Different Water Content on Rock Creep Law[J]. *J. China Coal Soc.* 32 (7), 698–702. doi:10.7520/1001-4888-15-241

Yang, Y., Sun, G., Zheng, H., and Yan, C. (2020). An Improved Numerical Manifold Method with Multiple Layers of Mathematical Cover Systems for the Stability Analysis of Soil-Rock-Mixture Slopes. *Eng. Geology.* 264, 105373. doi:10.1016/j.enggeo.2019.105373

Yin, Y. (2011). Recent Catastrophic Landslides and Mitigation in China. *J. Rock Mech. Geotechnical Eng.* 3, 10–18. doi:10.3724/sp.j.1235.2011.00010

Yin, Y., Sun, P., Zhang, M., and Li, B. (2011). Mechanism on Apparent Dip Sliding of Oblique Inclined Bedding Rockslide at Jiweishan, Chongqing, China. *Landslides* 8, 49–65. doi:10.1007/s10346-010-0237-5

Wei, Y. L., Yang, C. H., Guo, Y., Liu, W., Wang, L., and Heng, S. (2015). Experimental Investigation on Deformation and Fracture Characteristics of Brittle Shale with Natural Cracks under Uniaxial Cyclic Loading[J]. *Rock Soil Mech.* 36 (6), 1649–1658. doi:10.16285/j.rsm.2015.06.017

Zhang, M., McSaveney, M., Shao, H., and Zhang, C. (2018a). The 2009 Jiweishan Rock Avalanche, Wulong, China: Precursor Conditions and Factors Leading to Failure. *Eng. Geology.* 233, 225–230. doi:10.1016/j.enggeo.2017.12.010

Zhang, Y., Hu, X., Tannant, D. D., Zhang, G., and Tan, F. (2018b). Field Monitoring and Deformation Characteristics of a Landslide with Piles in the Three Gorges Reservoir Area. *Landslides* 15 (3), 581–592. doi:10.1007/s10346-018-0945-9

Zhou, C., Ying, C., Hu, X., Xu, C., and Wang, Q. (2020). Thermal Infrared Imagery Integrated with Multi-Field Information for Characterization of Pile-Reinforced Landslide Deformation. *Sensors (Basel)* 20, 1–7. doi:10.3390/s20041170

Zhu, B. L., Li, X. N., Wu, X. Y., and Wang, Y. J. (2015). Experimental Study of Micro-characteristics of Selling for Black Shale under Influence of Water[J]. *Chin. J. Rock Mech. Eng.* 34 (Z2), 3896–3905. doi:10.13722/j.cnki.jrme.2014.1147

Zin, A., Hawari, K., Hawari, K., and Khamisan, N. (2016). Early Detection of Spots High Water Saturation for Landslide Prediction Using Thermal Imaging Analysis. *Ijesd* 7 (1), 41–45. doi:10.7763/ijesd.2016.v7.738

Conflict of Interest: The authors declare that the research was conducted in the absence of any commercial or financial relationships that could be construed as a potential conflict of interest.